



# A data-driven surrogate modeling approach for time-dependent incompressible Navier-Stokes equations with dynamic mode decomposition and manifold interpolation

Martin W. Hess<sup>1</sup> · Annalisa Quaini<sup>2</sup> · Gianluigi Rozza<sup>1</sup> 

Received: 23 March 2022 / Accepted: 30 January 2023  
© The Author(s) 2023

## Abstract

This work introduces a novel approach for data-driven model reduction of time-dependent parametric partial differential equations. Using a multi-step procedure consisting of proper orthogonal decomposition, dynamic mode decomposition, and manifold interpolation, the proposed approach allows to accurately recover field solutions from a few large-scale simulations. Numerical experiments for the Rayleigh-Bénard cavity problem show the effectiveness of such multi-step procedure in two parametric regimes, i.e., medium and high Grashof number. The latter regime is particularly challenging as it nears the onset of turbulent and chaotic behavior. A major advantage of the proposed method in the context of time-periodic solutions is the ability to recover frequencies that are not present in the sampled data.

**Keywords** Spectral element method · Computational fluid dynamics · Model order reduction · Dynamic mode decomposition · Manifold interpolation

**Mathematics Subject Classification (2010)** 35Q35 65M22 76E30 76M22

---

Communicated by: Olga Mula

- ✉ Martin W. Hess  
mhess@sissa.it
- ✉ Annalisa Quaini  
quaini@math.uh.edu
- ✉ Gianluigi Rozza  
gianluigi.rozza@sissa.it

<sup>1</sup> mathLab, SISSA, via Bonomea, Trieste, 34136, Italy

<sup>2</sup> Department of Mathematics, University of Houston, Houston, TX 77204, USA

## 1 Introduction

Surrogate modeling, also known as reduced order modeling (ROM), is an invaluable tool for parameter studies of complex dynamical systems that has gained widespread use in recent decades (see [1–3]). In this work, we use a non-intrusive (i.e., data-driven) ROM approach, in the sense that only the field solutions of the equations governing the dynamical system at different time steps and parameter values are used to compute the surrogate model. Proper orthogonal decomposition (POD), dynamic mode decomposition (DMD), and manifold interpolation are combined into a novel multi-step approach, which allows to recover field solutions at parameters of interest. As is common for ROM methods, our approach adopts the offline-online decomposition. This means that during a time-intensive offline phase, all quantities needed for a fast evaluation of solutions over the parameter range are pre-computed from a few high-fidelity sample solutions. The offline phase can be performed on a high performance cluster, for example. The online phase, which computes the solution for parameters of interest that are not among the sample parameters, can be performed on a laptop or tablet.

To test and validate our ROM approach, we choose the Rayleigh-Bénard cavity problem with fixed aspect ratio and variable Grashof number (Gr), i.e., the nondimensional number that describes the ratio of buoyancy forces to viscous forces. Although this problem features only one physical parameter, it exhibits a wide range of patterns. At low Grashof numbers, the system has unique steady-state solutions. As Gr is increased, the system undergoes several Hopf bifurcations and multiple solutions arise for the same value of the Grashof number. Such solutions past the Hopf bifurcations are time-dependent: they are time-periodic at medium Grashof numbers and exhibit turbulent, chaotic behavior at very high Gr. A particular difficulty in applying a ROM approach to the Rayleigh-Bénard cavity over a large range of Gr is the following: the frequencies of time-periodic solutions at online parameters of interest are different from the frequencies at the sample solutions. We have tried several existing ROMs to address this difficulty and have not been successful. This motivated the work presented in this paper. The particular methodology we propose is targeted to problems featuring one or more Hopf bifurcations in the parameter domain of interest, the Rayleigh-Bénard cavity flow being one challenging example of such problems.

In the setting of bifurcating solutions, ROMs were first considered in [4–7] for buckling bifurcations in solid mechanics. More recently, in [8, 9], a reduced basis method is used to track solution branches from bifurcation points arising in natural convection problems. Reduced basis methods are also used in [10] to investigate Hopf bifurcations in natural convection problems and in [11] for symmetry breaking bifurcations in contraction-expansion channels. Recent works consider ROMs for bifurcating solutions in structural mechanics [12–14] and physics of condensates [15]. Finally, we would like to mention that machine learning techniques based on sparse optimization have been applied to detect bifurcating branches of solutions in

[16, 17] for a two-dimensional laterally heated cavity and Ginzburg-Landau model, respectively.

The work in this paper builds on our prior work [18, 19] and focuses on time-dependent solutions at higher Grashof number than previously investigated. At first, we tried the same approach as in [18], which uses artificial neural networks (ANNs) with multilayer perceptrons and different activation functions (like, e.g., ReLU) to improve the localized ROMs introduced in [19] (see also [20, 21] for more on POD with ANNs). However, it turned out that the time evolution of POD coefficients could not be well represented by this widely used class of ANNs. Then, we tried neural ODEs [22] and sparse identification of nonlinear dynamics [23], but still failed to recover the correct dynamics.

A major obstacle during the online phase is the correct interpolation of periodicity lengths at intermediate  $Gr$ . With increasing Grashof number, the periodicity length of the POD coefficients becomes smaller and the amplitude becomes larger. The associated flow becomes more complex in general, until it reaches chaotic and turbulent behavior at very large  $Gr$ . In principle, the DMD algorithm (see, e.g., [24–26]) is well-suited to resolve time-periodic evolution in a data-driven fashion [26]. However, the DMD solutions can not be interpolated to intermediate parameter configurations in a straightforward manner. In [27], the DMD is combined with a  $k$ -nearest neighbor regression to solve for new parameters of interest, while [28] considers several instances of DMD to solve for parametric problems. Other approaches [29, 30] use different approximation techniques (e.g., polynomial interpolation) and active subspaces to interpolate to new parameters. As mentioned earlier, the issue is that different frequencies are present at intermediate parameters than at the training samples. We propose to fix this issue by using manifold interpolation based on the DMD operators and DMD modes for interpolation at the new parameter values. With tangential interpolation based on [31], it is indeed possible to find intermediate frequencies reliably over a wide range of Grashof numbers, which is crucial to accurately recover the time-periodic solutions. A schematic of the method is reported in Fig. 1.

The rest of the paper is structured as follows. Section 2 introduces the variational formulation of the Navier-Stokes equations governing the Rayleigh-Bénard cavity and its discretization with the spectral element method. Section 3 explains the model reduction approach and Section 4 provides numerical results. In Section 5, we provide concluding remarks and further perspectives.

## 2 Rayleigh-Bénard cavity flow

We consider Rayleigh-Bénard cavity flow, introduced in [32] and widely studied since then (see, e.g. [10, 19, 33]) because of its rich bifurcating behavior, which includes several Hopf-type bifurcations. This flow is related to the Rayleigh-Bénard instability that arises in, e.g., semiconductor crystal growth [34]. Thus, although simplified, the Rayleigh-Bénard cavity flow is related to a practical engineering problem.

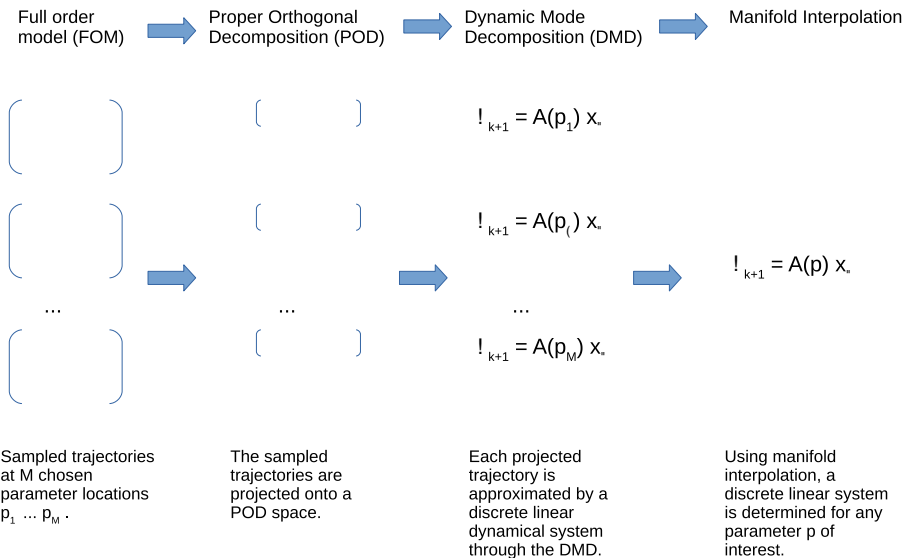


**Fig. 1** Schematic of the proposed three-stage ROM

## 2.1 Model description

The computational domain  $\Omega$  is a rectangular cavity with height 1 and length 4, i.e., with aspect ratio  $A = 4$ , filled with an incompressible, viscous fluid. The bottom left corner of the cavity is chosen as the origin of the coordinate system. The vertical walls are maintained at constant temperatures  $T_0$  (left wall) and  $T_0 + \Delta T$  (right wall) with  $\Delta T > 0$ , whereas the horizontal walls are thermally insulated.

This system over a time interval of interest  $(0, T)$  is governed by the incompressible *Navier-Stokes* equations

$$\frac{\partial \mathbf{u}}{\partial t} + \mathbf{u} \cdot \nabla \mathbf{u} = -\nabla p + \nu \Delta \mathbf{u} + (0, g\beta \Delta T(x/A)e_y)^T \quad \text{in } \Omega \times (0, T), \quad (1)$$

$$\nabla \cdot \mathbf{u} = 0 \quad \text{in } \Omega \times (0, T), \quad (2)$$

where  $\mathbf{u}$  is the vector-valued velocity,  $p$  is the scalar-valued pressure, and  $\nu$  is the kinematic viscosity. Moreover, in (1),  $g$  denotes the magnitude of the gravitational acceleration,  $\beta$  is the coefficient of thermal expansion,  $x$  is the horizontal coordinate, and  $e_y$  is the unit vector directed along the vertical axis. Problem (1)–(2) is endowed with boundary and initial conditions

$$\mathbf{u} = \mathbf{0} \quad \text{on } \partial\Omega \times (0, T), \quad (3)$$

$$\mathbf{u} = \mathbf{u}_0 \quad \text{in } \Omega \times 0, \quad (4)$$

with  $\mathbf{u}_0$  given.

The Grashof number

$$\text{Gr} = \frac{g\beta\Delta T}{A\nu^2} \quad (5)$$

characterizes the flow regime. The Grashof number describes the ratio of buoyancy forces to viscous forces. For large Grashof numbers (i.e.,  $\gg 1$ ), buoyancy forces are dominant over viscous forces and vice versa. Note that with (5) we can write the last term in (1) as  $(0, Gr\nu^2 x)^T$ . The Prandtl number for this problem is zero and the viscosity  $\nu$  is set to one.

As the Grashof number is increased, the sequence of events is as follows [32, 33]. For low Grashof number, a steady-state solution exists, which is characterized by a single primary circulation, also referred to as roll or convective cell. At a first bifurcation point, the steady-state single roll solution turns into a time-periodic solution and also a steady-state two roll solution appears around the same  $Gr$ . At higher Grashof number, the two roll solutions also turn from steady-state to time-periodic and a three roll steady-state solutions appear. With increasing  $Gr$ , this three roll steady-state solution will become time-dependent: time-periodic at first and then chaotic (i.e., without an obvious periodicity) upon a further increasing of  $Gr$ . The exact values of the Grashof number where the bifurcations occur depend on the aspect ratio  $A$  and other parameters, such as the Prandtl number.

## 2.2 Discretization

For the numerical solution of the eqs. (1)–(2), we adopt the PDE solver Nektar++. It employs a velocity correction scheme, which advances the nonlinear part explicitly in time and the linear part implicitly. This time-stepping is also known as a splitting scheme or IMEX (IMplicit-EXplicit) scheme [35, 36].

The computational domain is divided into 24 quadrilateral elements as shown in Fig. 2. We use modal Legendre ansatz functions of order 16, leading to 6321 global degrees of freedom for each scalar variable (i.e., horizontal velocity, vertical velocity, and pressure ansatz space, this is a standard option in Nektar++), which means a total of 18963 degrees of freedom.

We treat the Grashof number  $Gr$  as a parameter and assume it ranges over two intervals:  $[100e3, 150e3]$  and  $[650e3, 700e3]$ . In both intervals, three roll solutions are typically encountered. The velocity vector field at  $Gr = 100e3$  is shown in Fig. 3. Upon visual inspection of the flow field, no time-dependence can be detected. However, it is hard to determine numerically whether this solution is nearing a steady

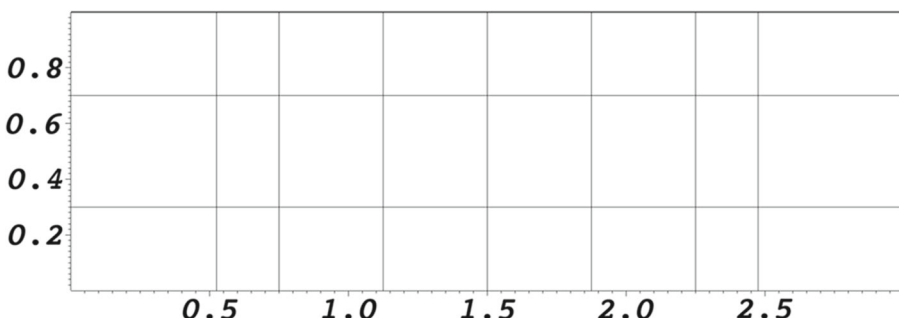


**Fig. 2** The 24 spectral elements used in the simulations, resulting in 18963 degrees of freedom

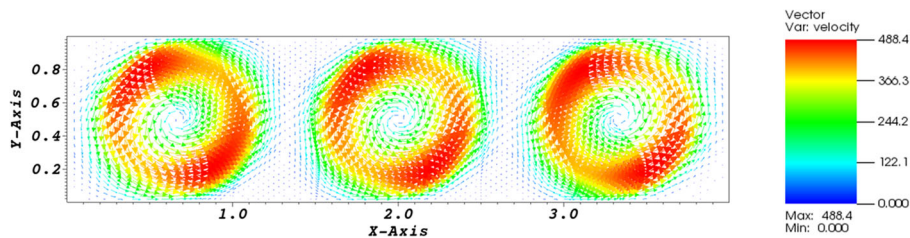


**Fig. 3** Velocity vector field at Grashof number  $1000e3$ . Color and length of a vector indicate velocity magnitude

state or is time-periodic since the convergence speed close to the critical value of  $Gr$  for the bifurcation point is very slow and a time-periodic pulsation with a very small amplitude around a mean field might also be possible. Figure 4 shows the time-periodic solution at  $Gr = 700e3$  for about two periods. Periodicity is easy to observe from the numerical solution. As the Grashof number increases, the period becomes shorter. For  $Gr > 700e3$ , chaotic behavior can be already observed. For example, at  $Gr = 1000e3$ , we observed that the POD coefficient of the first dominant mode can only be described as “noise,” which supports the impression from the velocity time evolution as chaotic. Of course, these are only numerical observations. There is no analytical proof.

Our numerical studies will focus on two distinct parameter domains. First, we will look at the interval  $[100e3, 150e3]$ , where the periods are rather large and the three roll time-dependent solutions have just occurred. A full-order solution is computed at  $Gr = 150e3$  over a long time interval to ensure that the limit cycle is reached. Then, each solution of interest in the interval  $[100e3, 150e3]$  is initialized with the solution at  $Gr = 150e3$ . The time step is set to  $1e-6$  and  $2e5$  time steps are computed. However, the first  $1e5$  time steps are disregarded in order to ensure that the solution is sufficiently close to its limit cycle for each parameter of interest. Next, we will consider interval  $[650e3, 700e3]$ , where the periods are short and the simulations are close to becoming chaotic. Thus, a smaller time step size of  $5e-7$  is used. We compute  $3e5$  time steps and disregard the first  $1e5$  time steps. In this second parameter interval, we first compute the full-order solution at  $Gr = 650e3$  and use it to initialize all the other solutions of interest.

### 3 A model order reduction approach

The offline phase of our model order reduction approach is articulated into two steps: (i) proper orthogonal decomposition (POD) briefly explained in Section 3.1 and (ii) dynamic mode decomposition (DMD) described in Section 3.2. For the online phase, we adopt manifold interpolation as explained in Section 3.3.

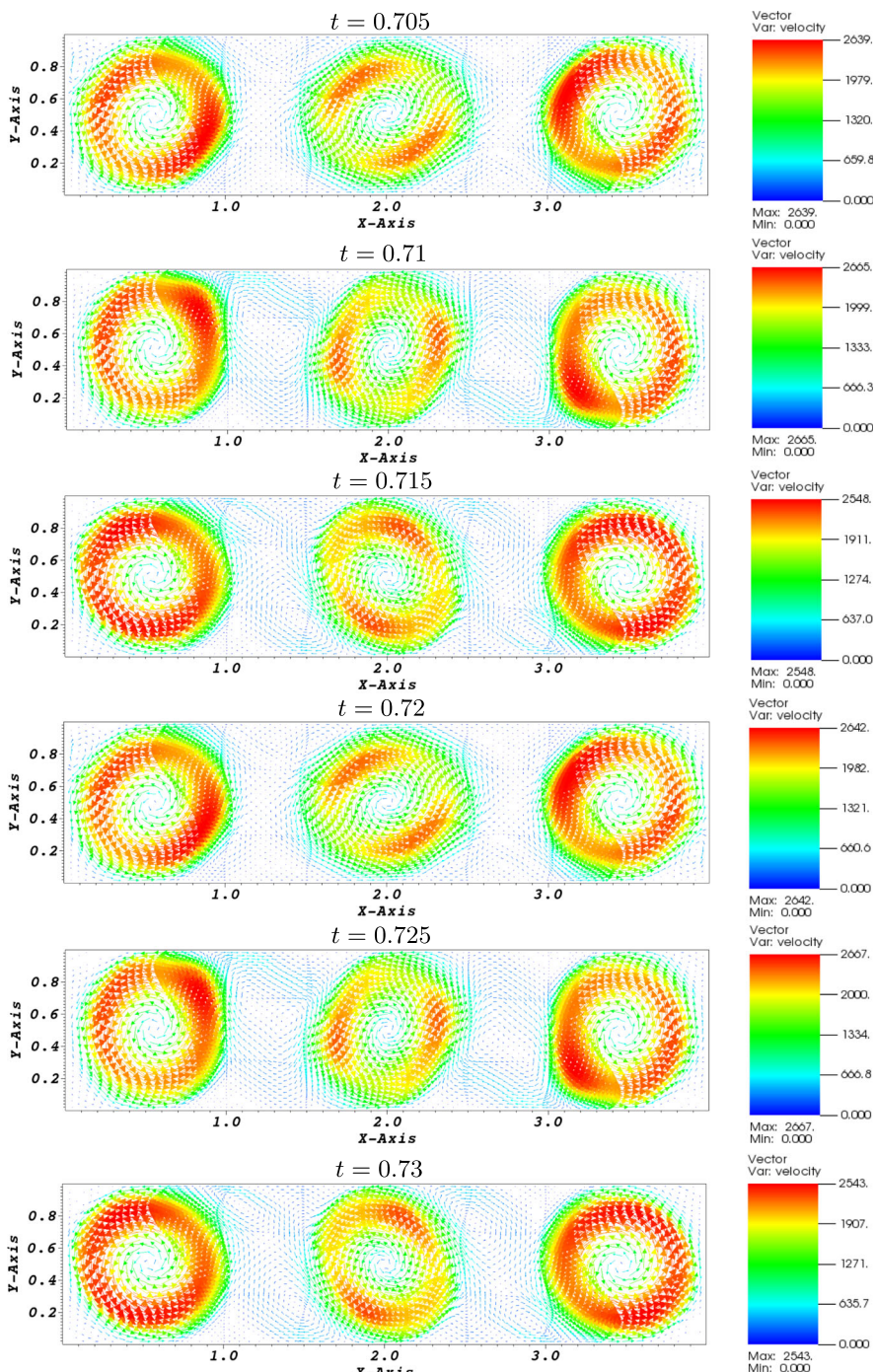


**Fig. 4** Time-periodic velocity vector field at Grashof number 700e3. Color and length of a vector indicate velocity magnitude. Shown are approximately two periods

### 3.1 Proper orthogonal decomposition

At each Grashof number, we collect the velocity field solutions at every time step in the time interval of interest. These real vectors of dimension  $\mathcal{N}$  ( $\mathcal{N}$  referring to size of the spatial discretization) form the trajectory for the given Grashof number. Our first goal is to find a projection matrix to reduce the large dimension  $\mathcal{N}$  to a lower dimension  $N$ . We achieve this through POD, which computes a projection space  $X_N$  used to project the trajectories for all parameters in the parameter domain of interest. Because of the very small time steps required by the cavity simulations, POD is just an initial data reduction step. A second reduction step is needed in order to contain the storage requirements for the trajectories (see Section 3.2).

The POD is based on an operator eigenvalue problem that reduces to the singular value decomposition for discrete data. Given a sample matrix  $S \in \mathbb{R}^{\mathcal{N} \times N}$ ,

compute the singular value decomposition as

$$S = U \Sigma V^T,$$

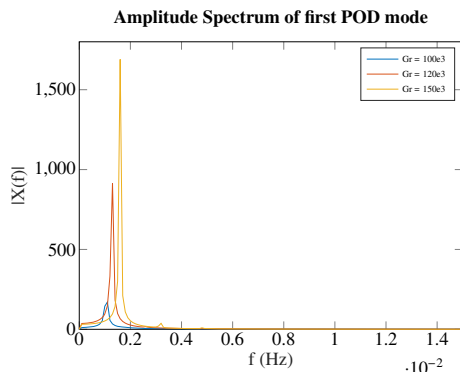
where  $\Sigma \in \mathbb{R}^{\mathcal{N} \times N}$  is a diagonal matrix with the (non-negative) singular values on the diagonal and  $U \in \mathbb{R}^{\mathcal{N} \times N}$  and  $V \in \mathbb{R}^{N \times N}$  are orthogonal. Assuming that the singular values are ordered in decreasing order, then the first columns of  $U$ , called left singular vectors, constitute the dominant POD modes. The most dominant POD modes are then used as basis functions for the reduced order projection space  $X_N$ . For the sake of brevity, we do not report here further details and refer the interested reader to textbooks, such as, [37].

The number of POD modes that are retained is typically determined by a threshold on the percentage of the sum of the singular values, e.g., 99%. In particular, if the prescribed threshold is met by the sum of the  $L$  largest singular values, but not by the sum of the  $L - 1$  largest singular values, then the  $L$  leftmost columns of  $U$  are used in the reduced order ansatz space  $X_N$  (see, e.g., [38], for more details and computational insights on POD in computational fluid dynamics).

The sample matrix  $S$  needs to cover the features of the time-dependent solutions over the parameter range in order for the resulting projection space  $X_N$  to retain such features. Because the problem under consideration leads to simulations with large time trajectories, we derive the sample matrix  $S$  in an adaptive fashion. For each full-order simulation, we first generate an intermediate matrix by following an adaptive snapshot selection strategy from [39]: we collect samples by adding time instants only if the angle to the already chosen time instants is over a given threshold.

POD is performed on the sampled time instants for each parameter location. Then, the dominant modes resulting from the POD for each parameter location are collected into a second sample matrix, separately for each velocity component. Then, a second application of POD defines the actual projection space  $X_N$  and can be understood as a compound POD space of the POD spaces for each time-trajectory. At the end of this first step, we obtain the time-trajectories at each sampled parameter location projected onto the space  $X_N$ .

**Fig. 5** Amplitude spectrum of the first POD mode for three values of the Grashof number in the medium Grashof interval



This two-tier procedure described in this section allows to keep the storage requirement low, such that the algorithms can even be executed on a common workstation. In fact, no more than 3 GB of RAM were necessary to hold a sampled time trajectory.

Figure 5 displays the spectrum of the first POD mode of the horizontal velocity component for Grashof numbers  $100e3$ ,  $120e3$ , and  $150e3$ . We observe that the dominant frequency increases with increasing Grashof number. At higher POD modes, more frequencies present, but with a smaller amplitude. Thus, they are less important for an accurate approximation (see Fig. 6 for the amplitude spectrum of the fifth and ninth POD mode of the horizontal velocity component for the same three Grashof numbers). The same conclusions (i.e., the frequencies increase with increasing Grashof number and more small amplitude frequencies are present in higher POD modes) hold for the high Grashof interval, although in this interval the dominant frequencies are higher and amplitudes are larger than in the medium Grashof interval (see Figs. 7 and 8). The amplitude spectra for the POD modes of the vertical velocity component are omitted because they look very similar to Figs. 5, 6, 7, and 8.

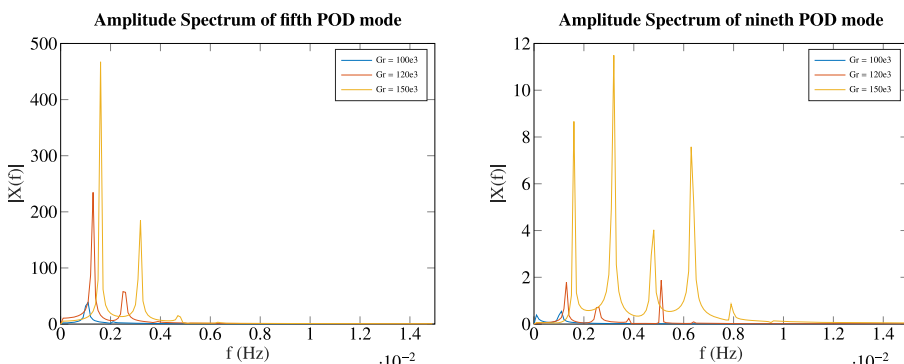


**Fig. 6** Amplitude spectrum of the fifth (left) and ninth (right) POD mode for three values of the Grashof number in the medium Grashof interval

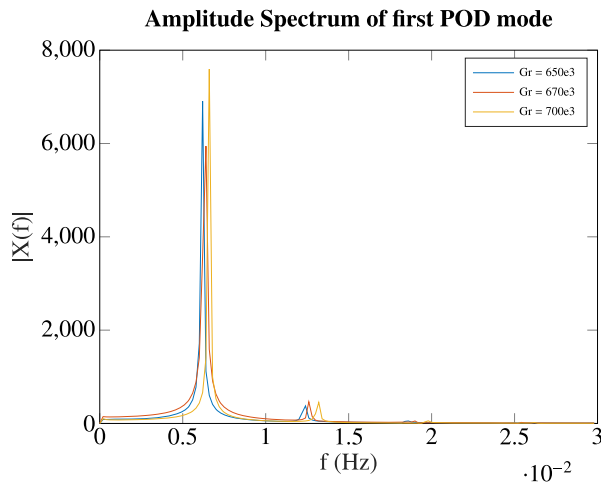


**Fig. 7** Amplitude spectrum of the first POD mode for three values of the Grashof number in the high Grashof interval

### 3.2 Dynamic mode decomposition

The POD procedure described in the previous section provides a projected trajectory that will take the role that is typically associated with the full-order trajectory in the DMD algorithm.

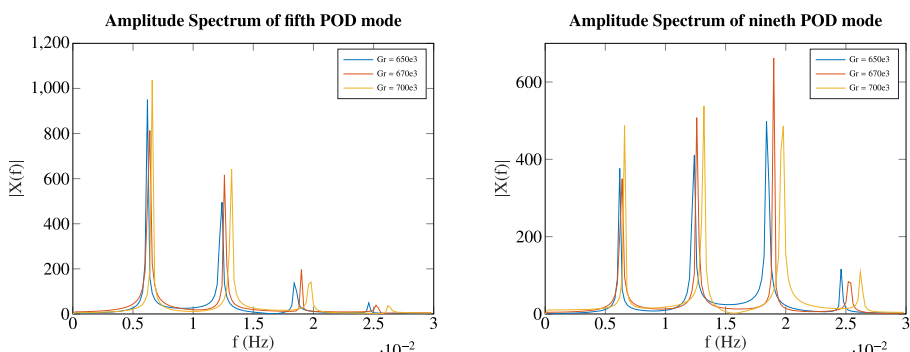


**Fig. 8** Amplitude spectrum of the fifth (left) and ninth (right) POD mode for three values of the Grashof number in the high Grashof interval

We refer the reader to [24–26] for an introduction to DMD. For its software implementation, in this work, we use PyDMD<sup>1</sup> [40].

Assume the time trajectory is given in the form of state variables  $(\mathbf{x}^k)_{k=1}^m \subset X_N$ , with  $m$  being the total number of time steps. The goal of DMD is to obtain a linear operator  $A \in \mathbb{R}^{N \times N}$ , which approximates the dynamics as

$$\mathbf{x}^{k+1} \approx A\mathbf{x}^k \quad \forall k = 1, \dots, m-1. \quad (6)$$

If we arrange the state vectors for  $k = 1, \dots, m-1$  column-wise in a matrix  $\mathbf{X}$  and the state vectors for  $k = 2, \dots, m$  column-wise in a matrix  $\mathbf{Y}$ , then (6) is equivalent to

$$\mathbf{Y} \approx A\mathbf{X}. \quad (7)$$

A best-fit approach computes  $A = YX^\dagger$ , where  $X^\dagger$  denotes the Moore-Penrose pseudoinverse of  $X$ . The linear predictor  $A$ , also called the *Koopman operator*, allows to recover an approximate trajectory by evaluating (6) starting from a given  $\mathbf{x}^1$ .

In order to have a reduced order computation of the trajectory, we first compute the rank  $r$  truncated singular value decomposition of  $X$  as  $X \approx U_r \Sigma_r V_r^T$ . The matrix  $U_r$  holds the real-valued DMD modes as columns. The reduced operator  $A_r \in \mathbb{R}^{r \times r}$  is defined as

$$A_r = U_r^T A U_r = U_r^T Y X^\dagger U_r = U_r^T Y V_r \Sigma_r^{-1} U_r^T U_r = U_r^T Y V_r \Sigma_r^{-1}, \quad (8)$$

where we have used the fact that  $U_r \in \mathbb{R}^{N \times r}$  is orthogonal. Matrix  $A_r$  is used for the reduced order computation of the trajectory as follows:

$$\mathbf{x}_r^{k+1} = A_r \mathbf{x}_r^k. \quad (9)$$

The full-order trajectory can be approximately recovered as  $\mathbf{x}^k = U_r \mathbf{x}_r^k$ .

There are many variants of DMD for different purposes. In this work, we use the real-valued standard DMD as shown in eq. (8) and (9). In fact, since the initial values of the provided trajectory samples are either on the limit cycle or close to it, the standard DMD is sufficient for an accurate reconstruction of the dynamics. However, if the interest is in recovering the trajectories from a common initial value for all parameters, then a variant of the DMD such as high-order DMD [41] or Hankel-DMD [42] can be used (see the PyDMD website for implementations and more details).

### 3.3 Manifold interpolation

During the online phase, one needs to evaluate the trajectory at a new parameter of interest. For this, we have to interpolate the reduced DMD operator, which requires a structure-preserving interpolation on nonlinear matrix manifolds. Manifold interpolation has been applied to many problems (see, e.g., [43–50]). Here, we briefly recapitulate the basics of manifold interpolation following [31].

As explained in Section 3.2, the DMD provides a reduced order representation of a trajectory at a fixed Grashof number. The idea is to sample some trajectories at different Grashof numbers, compute the DMD, and then interpolate the Koopman operator  $A$  to a new Grashof number of interest. In particular, the DMD modes  $U_r$  and

<sup>1</sup><https://github.com/mathLab/PyDMD>

the reduced DMD operator  $A_r$  will be interpolated independently<sup>2</sup> and then matrix  $A$  will be obtained using the relation

$$A = U_r A_r U_r^T. \quad (10)$$

A common picture in reduced basis model reduction is that of the solution manifold, where the solution vectors form a manifold in the ambient discrete space. Similarly, the reduced DMD operators define a manifold in the space of  $r \times r$  matrices. In particular, the reduced DMD operators will be understood as elements of the general linear group, which forms the manifold  $\mathcal{M}$ . Direct interpolation of matrix entries typically lead to poor results. Thus, interpolation is done on the tangent space  $T_p^{\mathcal{M}}$  for a base point  $p \in \mathcal{M}$ . Since the tangent space is flat, a direct interpolation with any interpolation algorithm that expresses the interpolant as a weighted sum of the samples is possible.

Let

$$\text{Log}_p^{\mathcal{M}} : \mathcal{M} \mapsto T_p^{\mathcal{M}}$$

be the Riemannian logarithm and

$$\text{Exp}_p^{\mathcal{M}} : T_p^{\mathcal{M}} \mapsto \mathcal{M}$$

the Riemannian exponential.

For a location  $p \in \mathcal{M}$ , the interpolation is performed following these steps:

- I1. Given a set of data points  $\{p_1, \dots, p_k\}$ , choose first a basis point  $p_i$ .
- I2. Check that  $\text{Log}_{p_i}^{\mathcal{M}}(p_j)$  is well-defined for all  $j = 1, \dots, k$  and compute  $v_j = \text{Log}_{p_i}^{\mathcal{M}}(p_j)$  for all  $j$ . Here,  $v_j = v(\text{Gr}_j)$  where  $\text{Gr}_j$  is the  $j$ th Grashof number sample location.
- I3. Compute  $v^*$  via Euclidean interpolation from the  $v_j$ , where  $v^*$  corresponds to the current Grashof number of interest, and interpolate the matrix entries according to the associated parameters.
- I4. Compute  $p^* = \text{Exp}_{p_i}^{\mathcal{M}}(v^*)$  as the interpolated matrix.

The above algorithm corresponds to Algorithm 7.1 in [31].

The reduced DMD operator is invertible, so a member of the general linear group of  $r \times r$  matrices  $GL(r)$ . Since  $GL(r)$  is open in the space of all  $r \times r$  matrices, the tangent space is simply the space of all  $r \times r$  matrices. The simplest choice for the Riemannian metric is the Euclidean metric, which gives a flat  $GL(r)$ . With this choice, the Riemannian exponential of  $D$  at a base point  $A_r \in GL(r)$  is given by

$$\text{Exp}_{A_r}(D) = A_r + D$$

and the Riemannian logarithm by

$$\text{Log}_{A_r}(\bar{D}) = \bar{D} - A_r.$$

Other options are possible for the Riemannian metric but will not be contemplated in this paper.

<sup>2</sup>Interpolating  $A$  directly does not seem promising. However, a possible alternative is to consider the DMD over the complex numbers, if the Riemannian metric is available.

The Grassmann manifold  $Gr(N, r)$  is the set of all  $r$ -dimensional subspaces  $\mathcal{U} \subset \mathbb{R}^N$ :

$$Gr(N, r) = \{\mathcal{U} \subset \mathbb{R}^N \mid \mathcal{U} \text{ subspace, } \dim(\mathcal{U}) = r\}.$$

It can be defined as a quotient manifold of the Stiefel manifold

$$St(N, r) = \{U \in \mathbb{R}^{N \times r} \mid U^T U = I_r\},$$

through

$$Gr(N, r) = St(N, r)/O(r) = \{[U] \mid U \in St(N, r)\},$$

where  $O(r)$  is the set of the orthogonal  $r \times r$  matrices and  $I_r$  the  $r \times r$  identity matrix. This means that a matrix  $U \in St(N, r)$  is the matrix representative of the subspace  $\mathcal{U} \in Gr(N, r)$  if  $\mathcal{U} = \text{range}(U)$ . The Grassmann manifold is a typical choice of manifold for projection matrices such as the matrix with POD modes as columns

because the choice of the basis is irrelevant, what matters is the space spanned by the vectors. Interpolation of the DMD modes is understood as interpolation on the Grassmann manifold.

The composition of the Riemannian exponential and logarithm gives the identity on  $Gr(N, r)$ . However, for the matrix representatives in  $St(N, r)/O(r)$ , the identity does not necessarily hold (see, e.g., [43] for an explanation on this). Thus, a modified algorithm for the logarithm is needed for the identity to hold at the matrix level. An example of such modified algorithm is provided in [31], Section 7.4.5.2. It reads as follows: Given a base point representative  $U \in St(N, r)$  of  $\mathcal{U} = [U] \in Gr(N, r)$  and a point on the manifold  $\tilde{\mathcal{U}} = [\tilde{U}] \in Gr(N, r)$  with representative matrix  $\tilde{U} \in St(N, r)$

L1. Compute the SVD of  $\tilde{U}^T U$  as

$$\Psi S R^T = \tilde{U}^T U.$$

L2. Transition to the Procrustes representative

$$\tilde{U}_* = \tilde{U} \Psi R^T,$$

and compute the intermediate matrix  $L$  as

$$L = (I_N - U U^T) \tilde{U}_*,$$

where  $I_N$  is the identity matrix.

L3. Compute the SVD of  $L$

$$Q \Sigma V^T = L.$$

L4. Compute the tangent vector  $\text{Log}_{\mathcal{U}}^{Gr}(\tilde{\mathcal{U}})$  on the tangent space  $T_{\mathcal{U}} Gr(N, r)$  as

$$\text{Log}_{\mathcal{U}}^{Gr}(\tilde{\mathcal{U}}) := Q \arcsin(\Sigma) V^T.$$

For a base point representative  $U \in St(N, r)$  of  $\mathcal{U} = [U] \in Gr(N, r)$  and a tangent vector  $\Delta \in T_{\mathcal{U}} Gr(N, r)$ , the exponential computes the point  $[\tilde{U}]$  on the Grassmann manifold. The algorithm is as follows:

E1. Compute the SVD of  $\text{Log}_{\mathcal{U}}^{Gr}(\tilde{\mathcal{U}})$  as

$$Q \Sigma V^T = \text{Log}_{\mathcal{U}}^{Gr}(\tilde{\mathcal{U}}).$$

E2. Compute  $[\tilde{U}]$  as

$$\tilde{U} = UV \cos(\Sigma)V^T + Q \sin(\Sigma)V^T.$$

## 4 Numerical results

As mentioned in Section 2.2, we will consider two parameter domains for the Grashof number  $\text{Gr}$ . The first domain is  $[100\text{e}3, 150\text{e}3]$  and the associated solutions show the onset of time-dependent three roll flow. Since previous works (e.g., [19, 33]) deals with lower values of  $\text{Gr}$ , this first interval is referred to as *medium Gr range*. The second domain is  $[650\text{e}3, 700\text{e}3]$ , with associated solutions that are close to the onset of turbulent and chaotic flow patterns. We will call this second interval *high Gr range*. Since the time of a single period decreases with increasing  $\text{Gr}$  and the flow becomes more complex, we expect that the values of  $\text{Gr}$  between the medium and high ranges can also be treated with the presented approach.

### 4.1 Medium Grashof range

The samples in the interval  $\text{Gr} \in [100\text{e}3, 150\text{e}3]$  are taken every  $10\text{e}3$ , i.e., we collect six samples in total. As explained in Section 3.1, we perform an adaptive POD for each trajectory and form the compound POD space for all sample trajectories. Both PODs use a threshold of 99.99% of the singular values, leading to a final dimension of 37 for the horizontal component of the velocity and 41 for the vertical component.

The DMD algorithm does not use all the POD modes. In fact, the DMD uses the first  $N = 30$  most dominant POD modes in both velocity directions and reduces the dimension to  $k = 10$  DMD modes. We found that in some cases a further restriction gives more accurate results. In particular, we inspected the first POD mode to check if it shows time-periodic behavior. This can be seen as an indication of accuracy since we expect to observe time-periodicity. If first POD mode is not time-periodic, a second DMD was computed with  $N = 10$  modes, which provided accurate results. The two values  $N = 30$  and  $N = 10$  have been determined empirically. In total, 20 DMDs are computed, i.e., two for each of the ten test samples for the horizontal and vertical component. The reduction to  $N = 10$  modes was applied in three cases.

As mentioned in Section 3.3, in order to compute the tangential interpolation, we need to choose a base point (step I1). This is a crucial choice since the results are quite sensitive to it. In fact, as one can expect, the interpolation is more accurate the closer the base point is to the online parameter of interest. Thus, for each online test parameter, we choose the closest sample point as base point. As for the interpolation technique, in principle, one can choose any technique that expresses the interpolant as a weighted sum of the samples. The first obvious choice to try is a linear interpolation between the two closest sample points. We found that linear interpolation gives very accurate results that usually cannot be improved by switching to a higher order interpolation or radial basis function interpolation. Thus, we

stuck to linear interpolation, which is actually identical to geodesic interpolation, see [31], Algorithm 7.2. Geodesic interpolation computes the unique geodesic between the subspaces corresponding to  $\text{Gr}_j$  and  $\text{Gr}_{j+1}$  for  $\text{Gr} \in [\text{Gr}_j, \text{Gr}_{j+1}]$ . In this particular case, it is possible to use either the subspace corresponding to  $\text{Gr}_j$  or  $\text{Gr}_{j+1}$  as base point, but care must be taken to use a consistent rotation to arrive at the same matrix representative.

In order to evaluate the accuracy of the ROM approach, we select pseudo-randomly ten test points in the interval  $\text{Gr} \in [100\text{e}3, 150\text{e}3]$ . By “pseudo-randomly,” we mean that we ensure that no test point coincides with a sample point and that the test points cover the entire parameter interval. For each test point, we compute the relative  $L^2(\Omega)$  and  $L^\infty(\Omega)$  error for the velocity for all time steps with respect to the full order simulation. We run the simulations for a total time  $T = 1\text{e}-1$  with time step  $1\text{e}-6$ . Since the DMD can not properly resolve the swing-in phase (the first  $1\text{e}5$  time steps), that is not considered for the error computations.

In this way, a start value close to the limit cycle is provided at each test point.

Table 1 reports the mean and maximum relative  $L^2(\Omega)$  and  $L^\infty(\Omega)$  error for the medium Grashof range and Fig. 9 visualizes the same data. We see that the three test points in-between sample points ( $\text{Gr} = 113.8\text{e}3$ ,  $\text{Gr} = 105.95\text{e}3$ , and  $\text{Gr} = 124.92\text{e}3$ ) have mean  $L^2(\Omega)$  and  $L^\infty(\Omega)$  errors up to 2.58%. All the remaining test points, which are closer to a sample point, have mean errors below 1%. The same observation holds true for the maximum error. In particular, we notice that the maximum  $L^\infty(\Omega)$  error for  $\text{Gr} = 105.95\text{e}3$  goes up to 8%. This shows that the distance to the base point is crucial for the accuracy of our approach, as mentioned above. Thus, we conclude that the proposed interpolation approach provides accurate approximations so long as the sample density is appropriate, i.e., there is a base point for the manifold interpolation near each new parameter value.

The relative  $L^2(\Omega)$  and  $L^\infty(\Omega)$  errors over time for the best approximated case ( $\text{Gr} = 129.26\text{e}3$ ) and the worst approximated case ( $\text{Gr} = 105.95\text{e}3$ ) amongst the test samples in Table 1 are shown in Fig. 10.

We see that at  $\text{Gr} = 129.26\text{e}3$ , there is no initial growth of the error over time in contrast to  $\text{Gr} = 105.95\text{e}3$ .

Let us take a look at the approximation of the first POD modes for the horizontal and vertical component of the velocity for both cases, which are reported in Fig. 11. In the case of  $\text{Gr} = 129.26\text{e}3$ , the error is dominated by the approximation in the vertical component since the first POD mode is well approximated for the horizontal component. Indeed, the blue line is superimposed to the red line in the top left panel in Fig. 11. Also at  $\text{Gr} = 105.95\text{e}3$ , the first POD mode is well approximated for the horizontal component, although the difference between approximated and reference mode becomes more evident as time passes. In addition, the mismatch between approximated and reference mode for the vertical component of the velocity is much larger at  $\text{Gr} = 105.95\text{e}3$  than at  $\text{Gr} = 129.26\text{e}3$ . For these two examples, the errors reported in Table 1 can be understood from the approximation of the first POD mode as shown in Fig. 11. For other values of  $\text{Gr}$ , it is necessary to also look at the other (less dominant) POD modes.

**Table 1** Mean and maximum relative errors for the velocity over  $T = 1e-1$ . The samples in the interval  $[100e3, 150e3]$  are taken every  $10e3$ 

	Gr= 113.8e3	Gr= 133.985e3	Gr= 132.755e3	Gr= 108.13e3	Gr= 105.95e3	Gr= 124.92e3	Gr= 147.98e3	Gr= 117.02e3	Gr= 129.26e3	Gr= 111.19e3
Mean $L^2$	0.0181	0.0072	0.0060	0.0070	0.0201	0.0153	0.0067	0.0074	0.0039	0.0046
Mean $L^\infty$	0.0222	0.0076	0.0062	0.0088	0.0258	0.0192	0.0071	0.0087	0.0041	0.0057
Max $L^2$	0.0399	0.0169	0.0139	0.0249	0.0628	0.0359	0.0174	0.0184	0.0104	0.0123
Max $L^\infty$	0.0497	0.0193	0.0152	0.0313	0.0798	0.0461	0.0207	0.0228	0.0122	0.0153

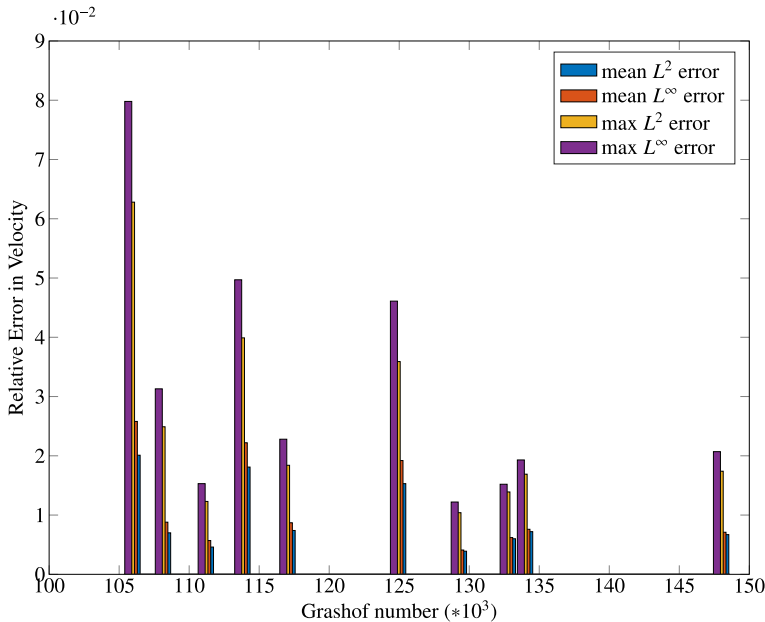


**Fig. 9** Bar plot visualizing the results from Table 1. The samples in the interval  $[100e3, 150e3]$  are taken every  $10e3$

## 4.2 High Grashof range

Following what we have done in the medium Grashof range, we take samples every  $10e3$  in the high Grashof range  $[650e3, 700e3]$  for a total of six samples. We repeat the two-tier POD procedure illustrated in Section 3.1 and set the threshold for both PODs to 99.99% of the singular values. The final dimensions are 78 for the horizontal velocity component and 82 for the vertical velocity component. Notice that the dimensions for both velocity components are larger than in the medium Grashof range.

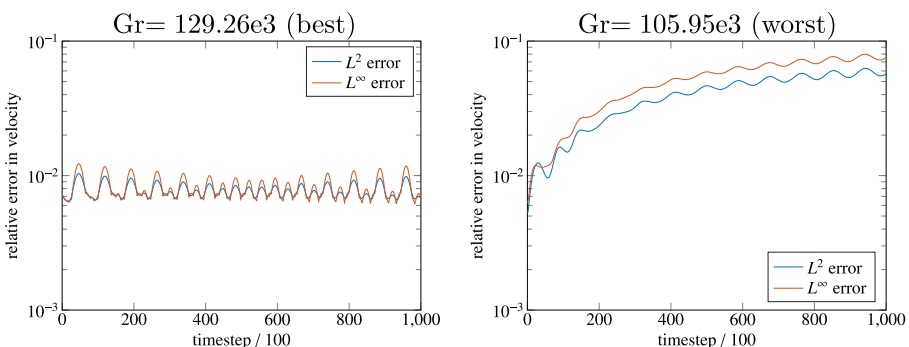


**Fig. 10** Relative errors over time for the velocity at  $Gr = 129.26e3$  (left) and  $Gr = 105.95e3$  (right)

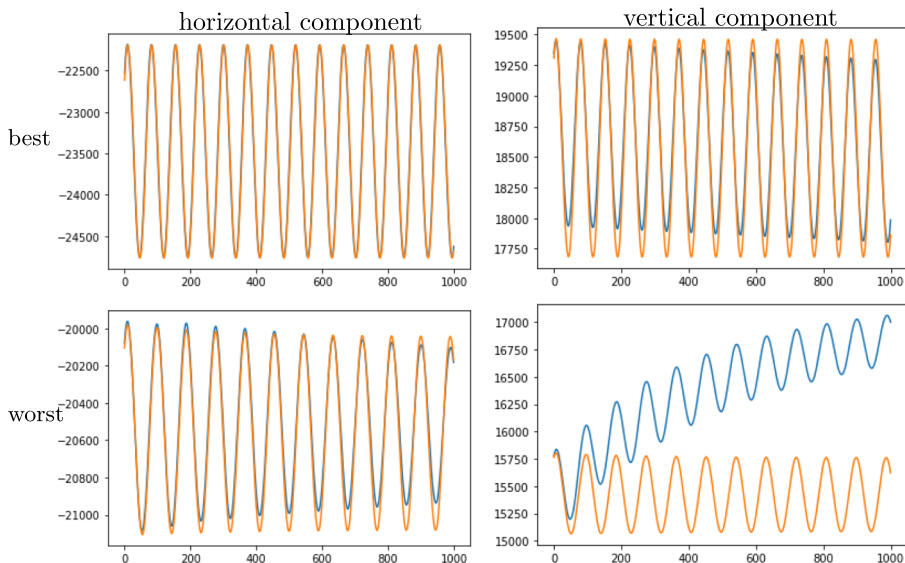


**Fig. 11** Approximation of the first POD mode coefficient (blue) and reference solution (red) for the horizontal (left) and vertical (right) component of the velocity in the best approximation case, i.e.,  $Gr=129.26e3$  (top), and worst approximation case, i.e.,  $Gr=105.95e3$  (bottom)

Just like for the medium Grashof range, the DMD uses the  $N = 30$  of the most dominant POD modes in both velocity directions and reduces to  $k = 10$  DMD modes. Moreover, if the first POD mode is not showing time-periodic behavior, the DMD algorithm is applied again with  $N = 10$ . This was used eight times out of 20 DMDs for the 10 test samples with independent DMDs for the horizontal and vertical component. Again, the manifold interpolation chooses the closest sample point as base point and uses linear interpolation in the tangent space.

The ten test points are chosen by shifting the ten random test points used for medium  $Gr$  interval to the high  $Gr$  interval  $Gr \in [650e3, 700e3]$ . For each test point, we compute the relative  $L^2(\Omega)$  and  $L^\infty(\Omega)$  error for the velocity for all time steps with respect to the full order simulation. Once again we remove the swing-in phase (the first  $1e5$  time steps) from the error computations, so that for each test point, a start value close to the limit cycle is provided. The error computation is then performed over another  $2e5$  time steps with a time step size of  $5e-7$  for a total time  $T = 1e-1$ .

Table 2 reports the mean and maximum relative  $L^2(\Omega)$  and  $L^\infty(\Omega)$  error for the velocity and Fig. 12 visualizes the same data. From this table, it is not easy to guess when an approximation is more or less accurate. The distance to the best point in the manifold interpolation does not seem to play the same obvious role as in the medium  $Gr$  range. For example, the mean  $L^2(\Omega)$  error is less than 6% for half the test points, while it goes up to about 15% for  $Gr=683.985e3$ . Similar observations can be made for the mean  $L^\infty(\Omega)$  error and the maximum errors.

**Table 2** Mean and maximum relative errors for the velocity over  $T = 1e-1$ . The samples in the interval [650e3, 700e3] are taken every 10e3

	Gr= 663.8e3	Gr= 683.985e3	Gr= 682.755e3	Gr= 658.13e3	Gr= 655.95e3	Gr= 674.92e3	Gr= 697.98e3	Gr= 667.02e3	Gr= 679.26e3	Gr= 661.19e3
Mean $L^2$	0.1136	0.1461	0.1197	0.0413	0.0428	0.0384	0.0970	0.1039	0.0426	0.0598
Mean $L^\infty$	0.1502	0.1956	0.1592	0.0454	0.0478	0.0404	0.1268	0.1365	0.0474	0.0735
Max $L^2$	0.1800	0.1846	0.1421	0.0504	0.0519	0.0438	0.1405	0.1681	0.0516	0.0975
Max $L^\infty$	0.2428	0.2488	0.1898	0.0575	0.0594	0.0472	0.1922	0.2264	0.0596	0.1295

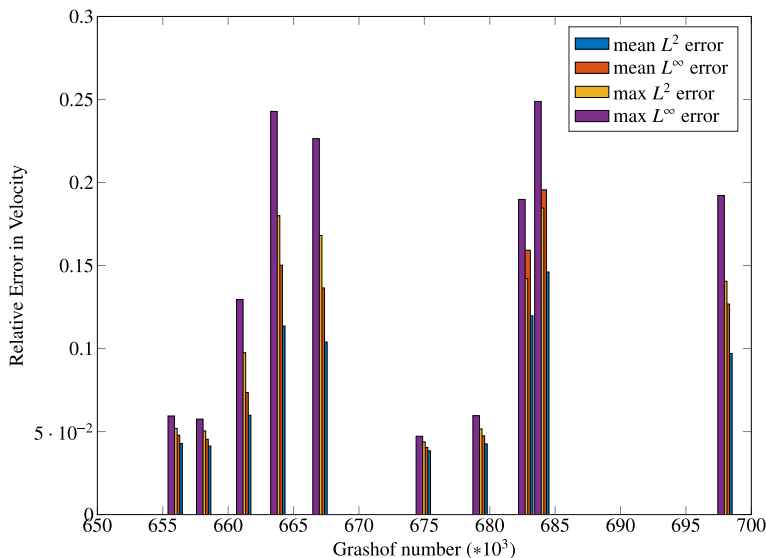


**Fig. 12** Bar plot visualizing the results from Table 2. The samples in the interval  $[650\text{e}3, 700\text{e}3]$  are taken every  $10\text{e}3$

The relative  $L^2(\Omega)$  and  $L^\infty(\Omega)$  errors over time for the best approximated case ( $\text{Gr} = 674.92\text{e}3$ ) and the worst approximated case ( $\text{Gr} = 683.985\text{e}3$ ) are shown in Fig. 13. The main qualitative difference is that at  $\text{Gr} = 674.92\text{e}3$  both the relative  $L^2(\Omega)$  and  $L^\infty(\Omega)$  errors oscillate around a fixed values, while at  $\text{Gr} = 683.985\text{e}3$ , they oscillate around a curved mean. An interesting feature of the errors at  $\text{Gr} = 683.985\text{e}3$  is that the maximum error is after about 1000 time steps and then the errors reduce again (see left panel in Fig. 13). This is due to the fact that the phase of the approximation is most out-of-sync at about time step 1000.

Once again, it is instructive to look at how the first POD modes for the horizontal and vertical components of the velocity are resolved in both cases (see Fig. 14). We see that at  $\text{Gr} = 674.92\text{e}3$ , the blue and red curves are practically superimposed

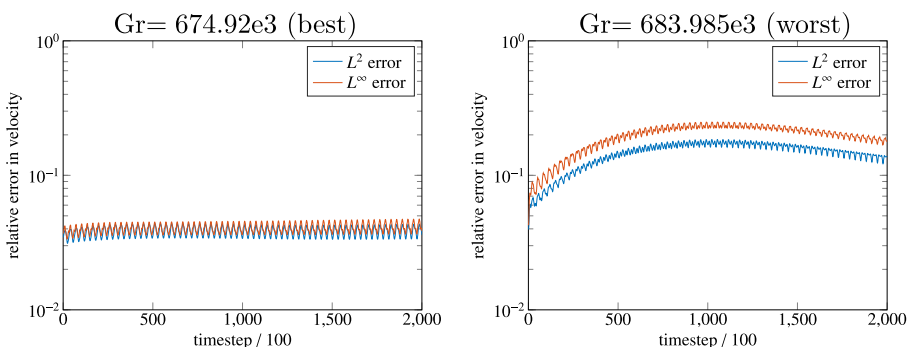


**Fig. 13** Relative errors over time for the velocity at  $\text{Gr} = 674.92\text{e}3$  (left) and  $\text{Gr} = 683.985\text{e}3$  (right)

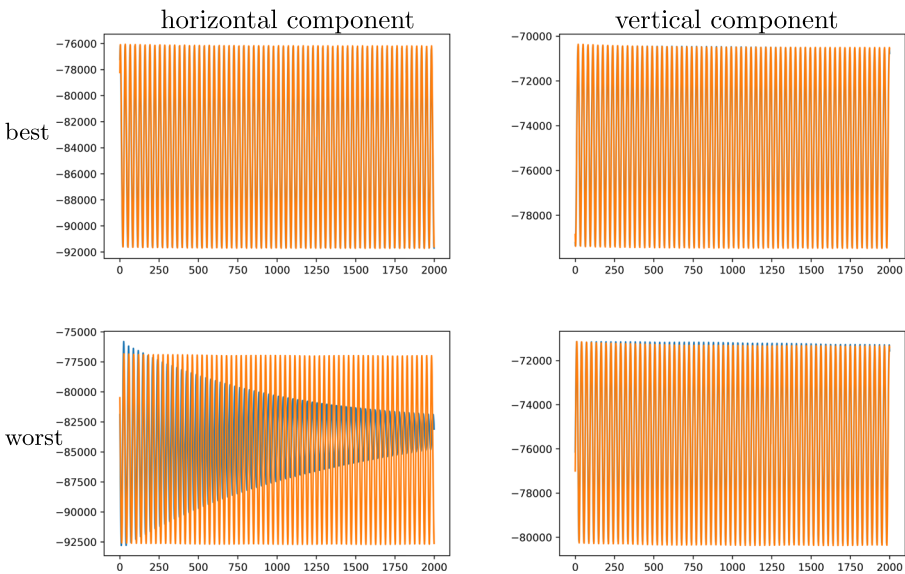


**Fig. 14** Approximation of the first POD mode coefficient (blue) and reference solution (red) for the horizontal (left) and vertical (right) component of the velocity in the best approximation case, i.e.,  $Gr=674.92e3$  (top), and worst approximation case, i.e.,  $Gr=683.985e3$  (bottom)

for both velocity components, indicating that error is negligible. Upon investigating the other POD modes, it becomes visible that the fourth mode for the vertical component of the velocity dominates the error (see Fig. 15). As for  $Gr=683.985e3$ , the error originates from the approximation of the first mode in the horizontal component as shown in the bottom left panel of Fig. 14. Although this panel shows that

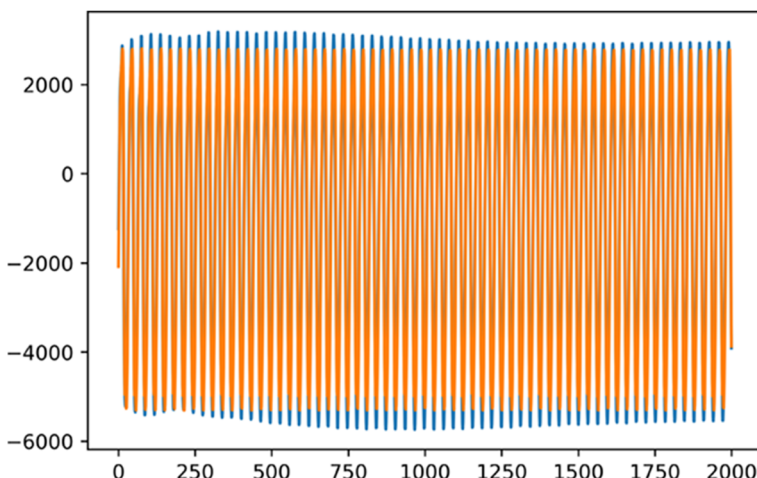


**Fig. 15** Approximation of the fourth POD mode coefficient (blue) and reference solution (red) in the vertical velocity component for  $Gr=674.92e3$

the horizontal component of the velocity at  $\text{Gr} = 683.985\text{e}3$  will not exhibit a time-periodic behavior, we could not find a number of POD modes and DMD modes to avoid this while keeping the same training samples. The accuracy could be improved by increasing the number of training samples.

Next, we report a qualitative comparison between solutions obtained with the full order model and our ROM approach at  $\text{Gr} = 674.92\text{e}3$  (in Fig. 16) and  $\text{Gr} = 683.985\text{e}3$  (in Fig. 17). Although at  $\text{Gr} = 674.92\text{e}3$ , the mean and maximum errors in  $L^2$  and  $L^\infty$  norms are between 3.5 and 5%, Fig. 16 shows that all important features have been captured by the ROM. On the other hand, Fig. 17 shows that the middle roll given by our ROM is out of phase with respect to the one in the full order solution. This could justify mean and maximum errors in  $L^2$  and  $L^\infty$  norms of about 14% and 25%, respectively, as reported in Table 2.

Although the higher accuracy in the medium Grashof range can be attributed to less complex high-order simulations, some additional comments are in order. Recall that in the  $100\text{e}3 - 120\text{e}3$  Grashof range, the solution is not too far from a steady state. Comparing the solution at fixed time  $t = 1\text{e}5$  produces 2–13% error, while our ROM method reduces this error to 2–4%, with the 2% lower bound arising from the POD projection error. In the high Grashof range, the ROM error is 2–15% on average, while comparing to the solution at fixed time  $t = 1\text{e}5$  produces an error of

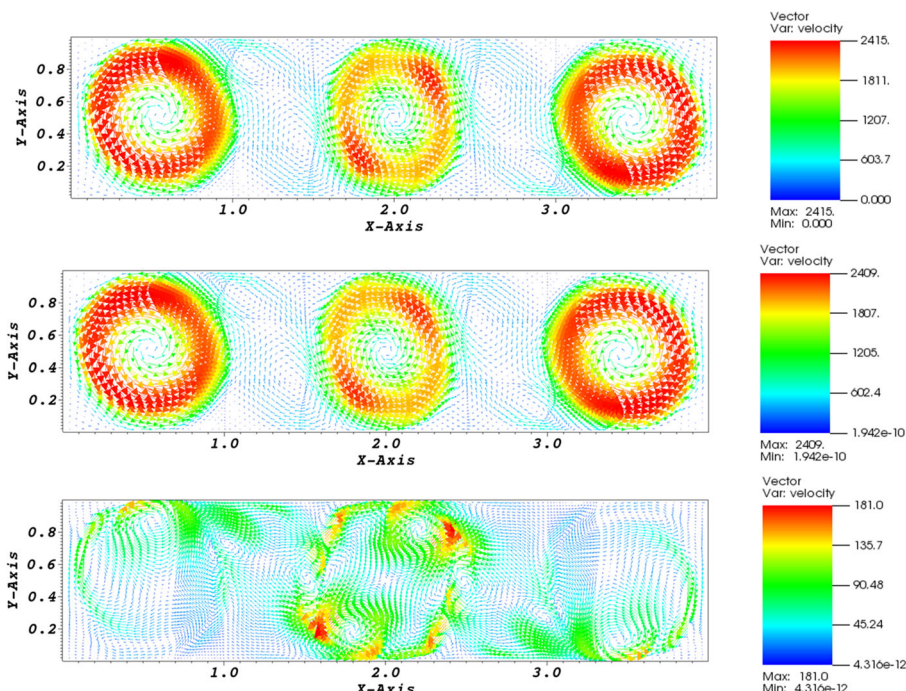


**Fig. 16** Comparison of the velocity vector field obtained with the full order model (top) versus our ROM approach (middle) and the difference of the two (bottom) at  $\text{Gr} = 674.92\text{e}3$  and after  $13\text{e}3$  time steps

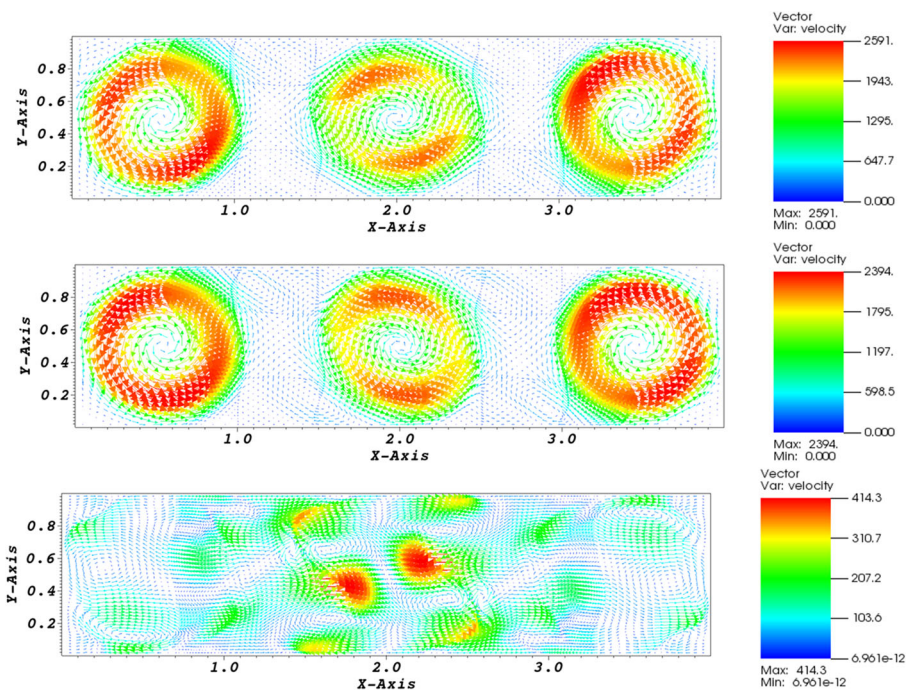


**Fig. 17** Comparison of the velocity vector field obtained with the full order model (top) versus our ROM approach (middle) and the difference of the two (bottom) at  $Gr = 683.985e3$  and after  $13e3$  time steps

2–35%. Thus, relative to the mean field solution, the model reduction works equally well in the medium and high  $Gr$  regimes.

We conclude this section by taking a look at the coefficients of the higher order modes. Figure 18 shows that such coefficients can have more complex features than the coefficients of the most dominant modes. Since the coefficients of the first modes usually have the largest amplitudes, these higher order modes are not well approximated by the DMD in general. However, it is more important to strive for

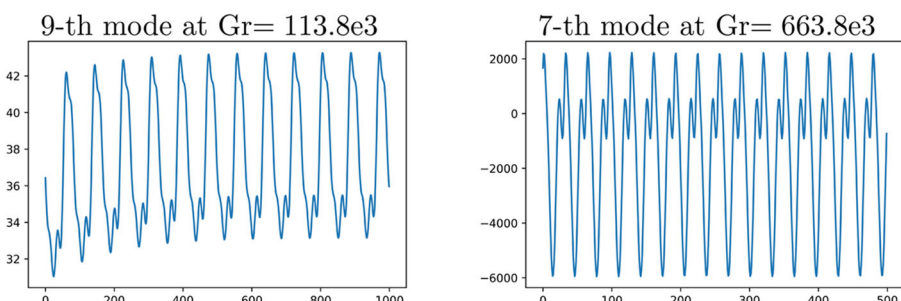


**Fig. 18** Evolution of the coefficient of the ninth mode at  $Gr = 113.8e3$  in  $y$ -direction (left) and seventh mode at  $Gr = 663.8e3$  in  $y$ -direction (right)

a low approximation error in the first, most dominant modes than to accurately reproduce the higher order modes.

## 5 Conclusions and future perspectives

This work introduces a data-driven ROM approach to compute efficiently complex time-periodic simulations. There are three main building blocks: proper orthogonal decomposition, dynamic mode decomposition (DMD), and manifold interpolation. Our ROM approach is tested and validated on the Rayleigh-Bénard cavity problem with fixed aspect ratio and variable Grashof number (Gr). We focus on two parameter domains with time-periodic solutions: a medium Gr range and a high Gr range, which is close to turbulent behavior. The key feature of our ROM is that it allows to recover frequencies not present in the sampled high-order solutions. This is crucial to achieve accurate simulations at new parameter values. Although in some instances of the high Gr regime, the mean relative error remained above 10%, most simulations achieved engineering accuracy.

Our multi-stage ROM method could be further improved as follows. Stability of the DMD algorithm could be enforced by various techniques employed in the DMD literature. The manifold interpolation might benefit from using non-flat metrics to interpolate the reduced DMD operator and the use of the complex DMD could be explored. Finally, it would be interesting to apply the proposed approach to other practical engineering problems and higher dimensional parameter domains as well as quasi-periodic systems.

**Funding** Open access funding provided by Scuola Internazionale Superiore di Studi Avanzati - SISSA within the CRUI-CARE Agreement. We acknowledge the support provided by the European Research Council Executive Agency by the Consolidator Grant project AROMA-CFD “Advanced Reduced Order Methods with Applications in Computational Fluid Dynamics” - GA 681447, H2020-ERC CoG 2015 AROMA-CFD, PI G. Rozza, and INdAM-GNCS 2019-2020 projects. This work was also partially supported by the US National Science Foundation through grant DMS-1953535. A. Quaini acknowledges support from the Radcliffe Institute for Advanced Study at Harvard University where she has been a 2021–2022 William and Flora Hewlett Foundation Fellow.

## Declarations

**Conflict of interest** The authors declare no competing interests.

**Open Access** This article is licensed under a Creative Commons Attribution 4.0 International License, which permits use, sharing, adaptation, distribution and reproduction in any medium or format, as long as you give appropriate credit to the original author(s) and the source, provide a link to the Creative Commons licence, and indicate if changes were made. The images or other third party material in this article are included in the article’s Creative Commons licence, unless indicated otherwise in a credit line to the material. If material is not included in the article’s Creative Commons licence and your intended use is not permitted by statutory regulation or exceeds the permitted use, you will need to obtain permission directly from the copyright holder. To view a copy of this licence, visit <http://creativecommons.org/licenses/by/4.0/>.

## References

1. Benner, P., Grivet-Talocia, S., Quarteroni, A., Rozza, G., Schilders, W., Silveira, L.M. (eds.): *Model Order Reduction: Volume 1: System- and Data-Driven Methods and Algorithms* De Gruyter. De Gruyter, Berlin, Boston (2021). <https://doi.org/10.1515/9783110498967>
2. Benner, P., Grivet-Talocia, S., Quarteroni, A., Rozza, G., Schilders, W., Silveira, L.M. (eds.): *Model Order Reduction: Volume 2: Snapshot-Based Methods and Algorithms* De Gruyter. De Gruyter, Berlin, Boston (2021). <https://doi.org/10.1515/9783110671490>
3. Benner, P., Grivet-Talocia, S., Quarteroni, A., Rozza, G., Schilders, W., Silveira, L.M. (eds.): *Model Order Reduction: Volume 3: Applications* D Gruyter. De Gruyter, Berlin, Boston (2021). <https://doi.org/10.1515/9783110499001>
4. Noor, A.: On making large nonlinear problems small. *Comput. Methods Appl. Mech. Eng.* **34**(1), 955–985 (1982)
5. Noor, A.: Recent advances and applications of reduction methods. *ASME Appl. Mech. Rev.* **5**(47), 125–146 (1994)
6. Noor, A., Peters, J.: Multiple-parameter reduced basis technique for bifurcation and post-buckling analyses of composite materials. *Int. J. Numer. Methods Eng.* **19**, 1783–1803 (1983)
7. Noor, A., Peters, J.: Recent advances in reduction methods for instability analysis of structures. *Comput. Struct.* **16**(1), 67–80 (1983)
8. Herrero, H., Maday, Y., Pla, F.: RB (reduced basis) for RB (Rayleigh-Bénard). *Comput. Methods Appl. Mech. Eng.* **261–262**, 132–141 (2013)
9. Pla, F., Herrero, H., Vega, J.: A flexible symmetry-preserving Galerkin/POD reduced order model applied to a convective instability problem. *Comput. Fluids* **119**, 162–175 (2015)
10. Pitton, G., Rozza, G.: On the application of reduced basis methods to bifurcation problems in incompressible fluid dynamics. *J. Sci. Comput.* **73**(1), 157–177 (2017)
11. Pitton, G., Quaini, A., Rozza, G.: Computational reduction strategies for the detection of steady bifurcations in incompressible fluid-dynamics: applications to Coanda effect in cardiology. *J. Comput. Phys.* **344**, 534–557 (2017)
12. Pichi, F., Rozza, G.: Reduced basis approaches for parametrized bifurcation problems held by nonlinear Von Kármán equations. *J. Sci. Comput.* **81**, 112–135 (2019). 10.1007/s10915-019-01003-3
13. Pichi, F., Strazzullo, M., Ballarin, F., Rozza, G.: Driving bifurcating parametrized nonlinear PDEs by optimal control strategies: application to Navier-Stokes equations with model order reduction. ArXiv preprint (2020)
14. Khamlich, M., Pichi, F., Rozza, G.: Model order reduction for bifurcating phenomena in fluid-structure interaction problems. ArXiv preprint (2021)
15. Pichi, F., Quaini, A., Rozza, G.: A reduced order modeling technique to study bifurcating phenomena: application to the Gross–Pitaevskii equation. *SIAM J. Sci. Comput.* **42**(5), 1115–1135 (2020)
16. Brunton, S.L., Tu, J.H., Bright, I., Kutz, J.N.: Compressive sensing and low-rank libraries for classification of bifurcation regimes in nonlinear dynamical systems. *SIAM J. Appl. Dyn. Syst.* **13**(4), 1716–1732 (2014). <https://doi.org/10.1137/130949282>
17. Kramer, B., Grover, P., Boufounos, P., Nabi, S., Benosman, M.: Sparse sensing and DMD-based identification of flow regimes and bifurcations in complex flows. *SIAM J. Appl. Dyn. Syst.* **16**(2), 1164–1196 (2017). <https://doi.org/10.1137/15M104565X>
18. Hess, M.W., Quaini, A., Rozza, G.: A comparison of reduced-order modeling approaches using artificial neural networks for PDEs with bifurcating solutions. *ETNA - Electronic Transactions on Numerical Analysis* **56**, 52–65 (2022). [https://doi.org/10.1553/etna\\_v56s52](https://doi.org/10.1553/etna_v56s52)
19. Hess, M.W., Alla, A., Quaini, A., Rozza, G., Gunzburger, M.: A localized reduced-order modeling approach for PDEs with bifurcating solutions. *Comput. Methods Appl. Mech. Engrg.* **351**, 379–403 (2019)
20. Hesthaven, J., Ubbiali, S.: Non-intrusive reduced order modeling of nonlinear problems using neural networks. *J. Comput. Phys.*, 363. <https://doi.org/10.1016/j.jcp.2018.02.037> (2018)
21. Pichi, F., Ballarin, F., Rozza, G., Hesthaven, J.S.: An artificial neural network approach to bifurcating phenomena in computational fluid dynamics. ArXiv preprint (2021)
22. Chen, R.T.Q., Rubanova, Y., Bettencourt, J., Duvenaud, D.: Neural ordinary differential equations. In: Proceedings of the 32nd International Conference on Neural Information Processing Systems. NIPS'18, pp. 6572–6583. Curran Associates Inc. (2018)

23. Brunton, S.L., Proctor, J.L., Kutz, J.N.: Discovering governing equations from data by sparse identification of nonlinear dynamical systems. *Proc. Natl. Acad. Sci.* **113**(15), 3932–3937 (2016). <https://doi.org/10.1073/pnas.1517384113>

24. Koopman, B.O.: Hamiltonian systems and transformation in Hilbert space. *Proc. Natl. Acad. Sci. U.S.A.* **17**(5), 315–318 (1931). <https://doi.org/10.1073/pnas.17.5.315>

25. Kutz, J.N., Brunton, S.L., Brunton, B.W., Proctor, J.L.: Dynamic mode decomposition society for industrial and applied mathematics. <https://doi.org/10.1137/1.9781611974508> (2016)

26. Schmid, P.J.: Dynamic mode decomposition of numerical and experimental data. *J. Fluid Mech.* **656**, 5–28 (2010). <https://doi.org/10.1017/S0022112010001217>

27. Gao, Z., Lin, Y., Sun, X., Zeng, X.: A reduced order method for nonlinear parameterized partial differential equations using dynamic mode decomposition coupled with k-nearest-neighbors regression. *J. Comput. Phys.* **452**(C), 110907 (2021). <https://doi.org/10.1016/j.jcp.2021.110907>

28. Sayadi, T., Schmid, P.J., Richecoeur, F., Durox, D.: Parametrized data-driven decomposition for bifurcation analysis, with application to thermo-acoustically unstable systems. *Phys. Fluids* **27**(3), 037102 (2015). <https://doi.org/10.1063/1.4913868>

29. Tezzele, M., Demo, N., Stabile, G., Mola, A., Rozza, G.: Enhancing CFD predictions in shape design problems by model and parameter space reduction. *Adv. Model. Simul. Eng. Sci.* **7**(40). <https://doi.org/10.1186/s40323-020-00177-y> (2020)

30. Andreuzzi, F., Demo, N., Rozza, G.: A dynamic mode decomposition extension for the forecasting of parametric dynamical system. ArXiv preprint (2021)

31. Zimmermann, R.: Manifold Interpolation. Volume 1 System- and Data-Driven Methods and Algorithms, pp. 229–274. De Gruyter. <https://doi.org/10.1515/9783110498967-007> (2021)

32. Roux, B. (ed.): Numerical Simulation of Oscillatory Convection in Low-Pr Fluids. Notes on Numerical Fluid Mechanics and Multidisciplinary Design, vol. 27. Springer, Vieweg+Teubner Verlag, Berlin (1990)

33. Gelfgat, A.Y., Bar-Yoseph, P.Z., Yarin, A.L.: Stability of multiple steady states of convection in laterally heated cavities. *J. Fluid Mech.* **388**, 315–334 (1999)

34. Kakimoto, K.: Flow instability during crystal growth from the melt. *Prog. Cryst. Growth Charact. Mater.* **30**(2), 191–215 (1995). [https://doi.org/10.1016/0960-8974\(94\)00013-J](https://doi.org/10.1016/0960-8974(94)00013-J)

35. Guermond, J.L., Shen, J.: Velocity-correction projection methods for incompressible flows. *SIAM J. Numer. Anal.* **41**(1), 112–134 (2003)

36. Karniadakis, G.E., Orszag, S.A., Israeli, M.: High-order splitting methods for the incompressible Navier-Stokes equations. *J. Comput. Phys.* **97**, 414–443 (1991)

37. Hesthaven, J., Rozza, G., Stamm, B.: Certified reduced basis methods for parametrized partial differential equations Springer (2015)

38. Lassila, T., Manzoni, A., Quarteroni, A., Rozza, G.: Model Order Reduction in Fluid Dynamics: Challenges and Perspectives. In: Quarteroni, A., Rozza, G. (eds.) Reduced Order Methods for Modeling and Computational Reduction. Modeling, Simulation and Applications, vol. 9, pp. 235–273. Springer, Milano (2014). Chap 9

39. Benner, P., Feng, L., Li, S., Zhang, Y.: Reduced-Order Modeling and Rom-Based Optimization of Batch Chromatography. In: Abdulle, A., Deparis, S., Kressner, D., Nobile, F., Picasso, M. (eds.) Numerical Mathematics and Advanced Applications - ENUMATH 2013, pp. 427–435. Springer (2015)

40. Demo, N., Tezzele, M., Rozza, G.: Pydmd: python dynamic mode decomposition. *J. Open Source Softw.* **3**(22), 530 (2018). <https://doi.org/10.21105/joss.00530>

41. Le Clainche, S., Vega, J.M.: Higher order dynamic mode decomposition. *SIAM J. Appl. Dyn. Syst.* **16**(2), 882–925 (2017)

42. Arbabi, H., Mezić, I.: Ergodic theory, dynamic mode decomposition, and computation of spectral properties of the Koopman operator. *SIAM J. Appl. Dyn. Syst.* **16**(4), 2096–2126 (2017). <https://doi.org/10.1137/17M1125236>

43. Amsallem, D., Farhat, C.: An online method for interpolating linear parametric reduced-order models. *SIAM J. Sci. Comput.* **33**(5), 2169–2198 (2011). <https://doi.org/10.1137/100813051>

44. Benner, P., Gugercin, S., Willcox, K.: A survey of projection-based model reduction methods for parametric dynamical systems. *SIAM Rev.* **57**(4), 483–531 (2015). <https://doi.org/10.1137/130932715>

45. Degroote, J., Vierendeels, J., Willcox, K.: Interpolation among reduced-order matrices to obtain parameterized models for design, optimization and probabilistic analysis. *Int. J. Numer. Methods Fluids* **63**(2), 207–230 (2010). <https://doi.org/10.1002/fld.2089>

46. Farhat, C., Grimberg, S., Manzoni, A., Quarteroni, A.: Computational Bottlenecks for PROMs: Pre-computation and Hyperreduction. Volume 2: Snapshot-Based Methods and Algorithms, pp. 181–244. De Gruyter. <https://doi.org/10.1515/9783110671490-005> (2021)
47. Loiseau, J.-C., Brunton, S.L., Noack, B.R.: From the POD-Galerkin Method to Sparse Manifold Models. Volume 3: Applications, pp. 279–320. De Gruyter. <https://doi.org/10.1515/9783110499001-009> (2021)
48. Peuscher, H., Mohring, J., Eid, R., Lohmann, B.: Parametric model order reduction by matrix interpolation. *Automatisierungstechnik* **58**, 475–484 (2010). <https://doi.org/10.1524/auto.2010.0863>
49. Zimmermann, R.: A locally parametrized reduced-order model for the linear frequency domain approach to time-accurate computational fluid dynamics. *SIAM J. Sci. Comput.* **36**(3), 508–537 (2014). <https://doi.org/10.1137/130942462>
50. Giovanis, D.G., Shields, M.D.: Data-driven surrogates for high dimensional models using gaussian process regression on the Grassmann manifold. *Comput. Methods Appl. Mech. Eng.* **370**, 113269 (2020). <https://doi.org/10.1016/j.cma.2020.113269>

**Publisher's note** Springer Nature remains neutral with regard to jurisdictional claims in published maps and institutional affiliations.